东南大学图书馆
Southeast University Library

东图学术快报
Academic express of SEU LIB

前沿经典　学科热点

学术动态　工具助手

编者按：“学术快报”是图书馆学科馆员利用 WOS/ESI/Incites、Scopus/SciVal 等权威数据库和分析工具，通过筛选研究前沿、跟踪重要学术网站，分专题进行编译报道的服务，方便我校师生快速了解国内外学术前沿、经典及热点，获取最新学术动态。

本期梳理 3 月 Nature、Science 期刊上材料科学领域的最新论文。

CONTACT US

联系电话：025-52090336-817

办公地址：李文正图书馆 B401 室

本期编辑：刘丽娟

本期审核：陆　美

美国 Science（《科学》）、英国 Nature（《自然》）及美国 Cell（《细胞》）是国际公认的三大享有最高学术声誉的科技期刊，发表在这三大期刊上的论文简称 CNS 论文。本次精选 2021 年 3 月 Science 和 Nature 中的部分材料科学论文，详细情况如下。

材料科学 3 月 Science 论文

[1]**Stabilizing black-phase formamidinium perovskite formation at room temperature and high humidity**

室温高湿条件下稳定黑相甲酰胺钙钛矿的形成

出版信息：Science 26 Mar 2021: Vol. 371, Issue 6536, pp. 1359-1364

作者：Wei Hui, Lingfeng Chao, Hui Lu, Fei Xia, et al.

第一作者单位：Key Laboratory of Flexible Electronics (KLoFE) and Institute of Advanced Materials (IAM), Nanjing Tech University, 30 South Puzhu Road, Nanjing 211816, Jiangsu, China.

国内相关报道：http://www.njtech.edu.cn/info/1058/2182212.htm

全文链接：https://science.sciencemag.org/content/371/6536/1359

Abstract：The stabilization of black-phase formamidinium lead iodide (α-FAPbI3) perovskite under various environmental conditions is considered necessary for solar cells. However, challenges remain regarding the temperature sensitivity of α-FAPbI3 and the requirements for strict humidity control in its processing. Here we report the synthesis of stable α-FAPbI3, regardless of humidity and temperature, based on a vertically aligned lead iodide thin film grown from an ionic liquid, methylamine formate. The vertically grown structure has numerous nanometer-scale ion channels that facilitate the permeation of formamidinium iodide into the lead iodide thin films for fast and robust transformation to α-FAPbI3. A solar cell with a power-conversion efficiency of 24.1% was achieved. The unencapsulated cells retain 80 and 90% of their initial efficiencies for 500 hours at 85° C and continuous light stress, respectively.

摘要翻译：黑相甲酰胺铅碘（α-FAPbI3）钙钛矿在各种环境条件下的稳定被认为是太阳能电池的必要条件。然而，在α-FAPbI3 的温度敏感性和其加工过程中严格控制湿度的要求方面仍然存在挑战。这里，我们报道不考虑湿度和温度的稳定α-FAPbI3 的合成，基于从离子液体甲酸甲胺中生长的垂直排列的碘化铅薄膜。

这种垂直生长的结构具有许多纳米级离子通道，这些通道有助于碘化甲酰胺渗透到碘化铅薄膜中，从而快速、稳定地转化为α-FAPbI3。我们获得了功率转换效率为 24.1%的太阳能电池。未封装的电池在 85° C 和连续光胁迫条件下分别保持了 80%和 90%的初始效率。

文中插图：

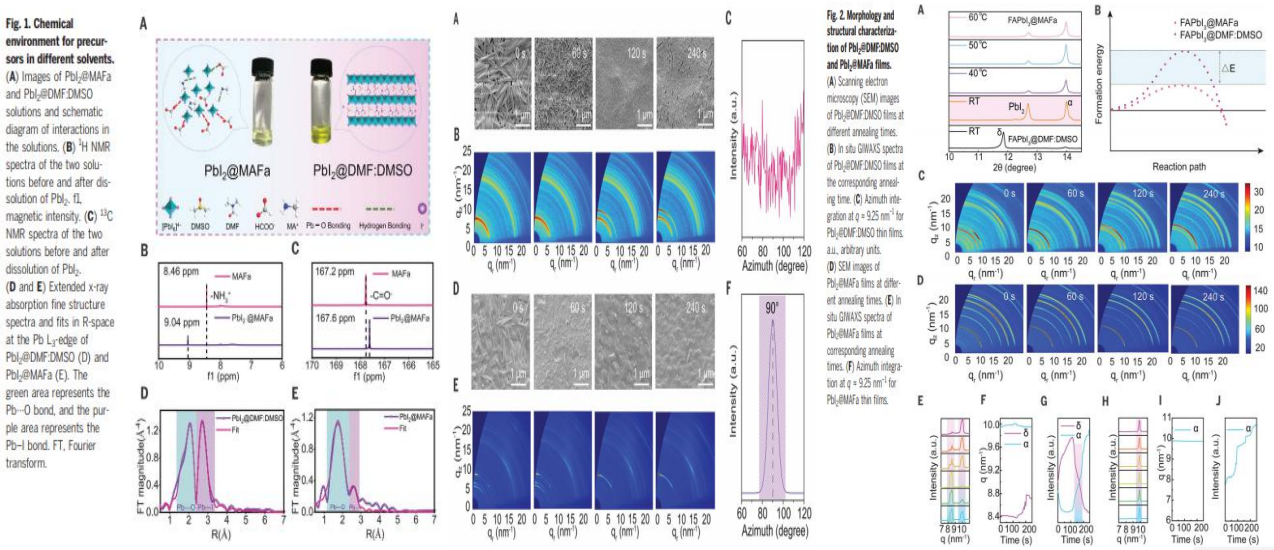

[2]Three-dimensional vectorial imaging of surface phonon polaritons

表面声子-极化子的三维矢量成像

出版信息：Science 26 Mar 2021:Vol. 371, Issue 6536, pp. 1364-1367

作者：Xiaoyan Li, Georg Haberfehlner, Ulrich Hohenester, Odile Stéphan, et al.

第一作者单位：Université Paris-Saclay, CNRS, Laboratoire de Physique des Solides, 91405 Orsay. France.

全文链接：https://science.sciencemag.org/content/371/6536/1364

Abstract：Surface phonon polaritons (SPhPs) are coupled photon-phonon excitations that emerge at the surfaces of nanostructured materials. Although they strongly influence the optical and thermal behavior of nanomaterials, no technique has been able to reveal the complete three-dimensional (3D) vectorial picture of their electromagnetic density of states. Using a highly monochromated electron beam in a scanning transmission electron microscope, we could visualize varying SPhP signatures from nanoscale MgO cubes as a function of the beam position, energy loss, and tilt angle. The SPhPs' response was described in terms of eigenmodes and used to tomographically reconstruct the phononic surface electromagnetic fields of the object. Such 3D information promises insights in nanoscale physical phenomena and is invaluable to the design and optimization of nanostructures for fascinating new uses.

摘要翻译：表面声子-极化子（SPhPs）是出现在纳米结构材料表面的光子-声子耦合激发。尽管它们强烈地影响纳米材料的光学和热行为，但没有一种技术能够揭示它们的电磁状态密度的完整三维(3D)矢量图。
在扫描透射电子显微镜中使用高度单色的电子束，我们可以将纳米级 MgO 立方体中不同的 SPhP 信号看作是光束位置、能量损失和倾斜角度的函数。将 SPhPs 的响应描述为本征模态，并用于声子表面电磁场的层析重建。
这样的三维信息为纳米尺度物理现象的研究提供了广阔的前景，并且对于纳米结构的设计和优化具有非常重要的价值。

文中插图：

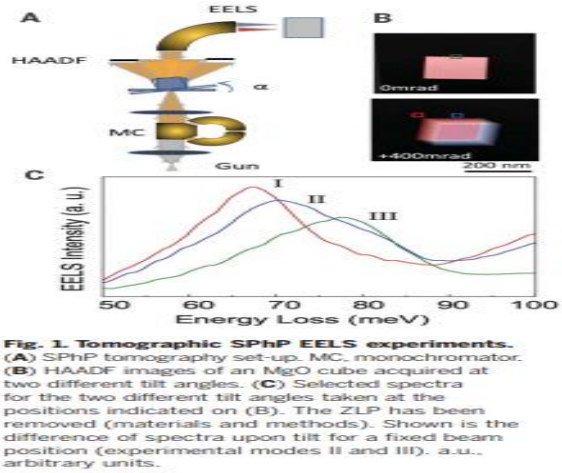

Fig. 1. Tomographic SPhP EELS experiments. (**A**) SPhP tomography set-up. MC, monochromator. (**B**) HAADF images of an MgO cube acquired at two different tilt angles. (**C**) Selected spectra for the two different tilt angles taken at the positions indicated on (B). The ZLP has been removed (materials and methods). Shown is the difference of spectra upon tilt for a fixed beam position (experimental modes II and III). a.u., arbitrary units.

Fig. 2. 2D phonon mapping at different tilt angles. (**A**) (Left) Experimental HAADF images and (right) fitted maps of the main experimental SPhP modes (I, II, and III) for two tilt configurations (0 and 400 mrad) (materials and methods). The face in contact with the substrate is highlighted with a blue square. (**B**) Same for simulations of a cube in vacuum.

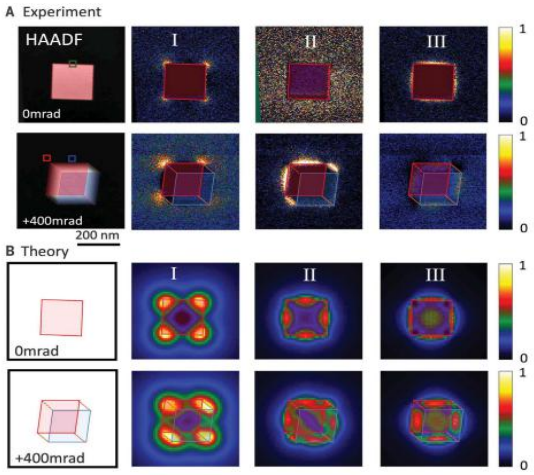

Fig. 3. 3D, fully vectorial reconstruction of the phononic electromagnetic local density of state. (**A**) NMF components extracted from the experimental data. (**B**) Reconstructed NMF maps for the three components at the two angles shown in Fig. 2. (**C**) 3D reconstruction of the EMLDOS seen from the top (the substrate, not shown, is at the bottom of the cube). The polarization of the EMLDOS along three orthogonal directions is shown as needles, in which color and length indicate its intensity.

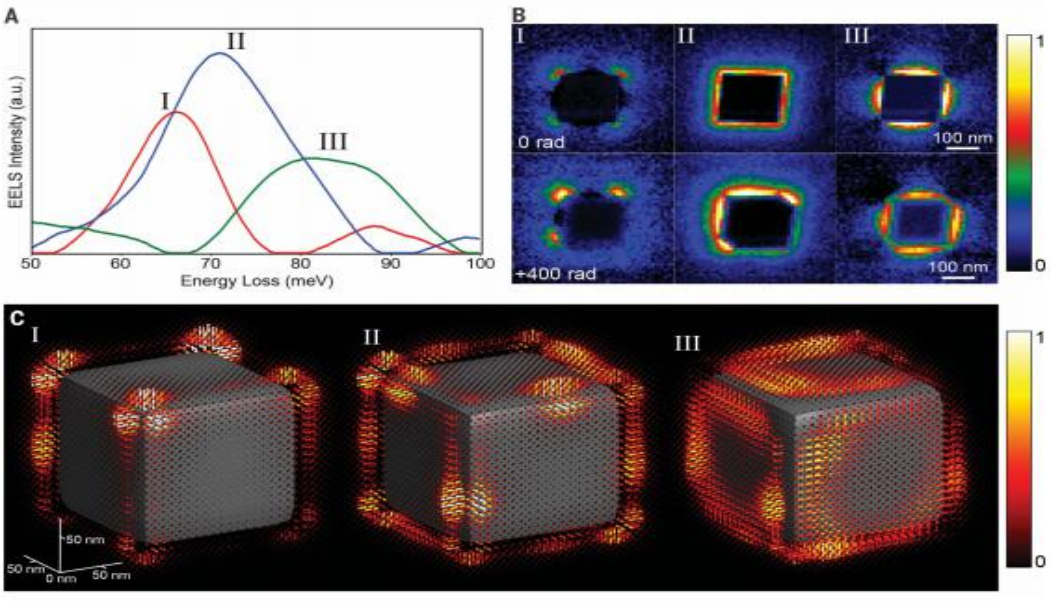

[3]Enhanced optical asymmetry in supramolecular chiroplasmonic assemblies with long-range order

超分子等离子组合物的增强光学不对称性

出版信息：Science　26 Mar 2021:Vol. 371, Issue 6536, pp. 1368-1374

作者：Jun Lu, Yao Xue, Kalil Bernardino, Ning-Ning Zhang, Weverson R. Gomes, et al.

第一作者单位：State Key Laboratory of Supramolecular Structure and Materials, College of Chemistry, Jilin University, Changchun, China.

国内相关报道：http://chem.jlu.edu.cn/info/1084/9991.htm

全文链接：https://science.sciencemag.org/content/371/6536/1368

Abstract：Chiral assemblies of plasmonic nanoparticles are known for strong circular dichroism but not for high optical asymmetry, which is limited by the unfavorable combination of electrical and magnetic field components compounded by strong scattering. Here, we show that these limitations can be overcome by the long-range organization of nanoparticles in a manner similar to the liquid crystals and found in helical assemblies of gold nanorods with human islet amyloid polypeptides. A strong, polarization-dependent spectral shift and the reduced scattering of energy states with antiparallel orientation of dipoles activated in assembled helices increased optical asymmetry g-factors by a factor of more than 4600. The liquid crystal–like color variations and the nanorod-accelerated fibrillation enable drug screening in complex biological media. Improvement of long-range order can also provide structural guidance for the design of materials with high optical asymmetry.

摘要翻译：等离子体纳米粒子的手性组装具有较强的圆二色性，而不具有较强的光学不对称性，这是由于强散射所造成的电场和磁场组合的不利限制。在此，我们证明了这些限制可以通过类似于液晶的纳米颗粒的长程组织方式来克服。这种组织方式类似于液晶，并在金纳米棒与人类胰岛淀粉样多肽的螺旋组合中发现。在组装螺旋中激活的具有反平行方向的偶极子的强大的、偏振相关的光谱偏移和能量态的减少散射使光学不对称性 g 因子增加了超过 4600 倍。这种类似液晶的颜色变化和纳米棒加速的纤维性颤动使药物在复杂的生物介质中筛选成为可能。长程序的改进也可以为高光学不对称材料的设计提供结构指导。

文中插图：

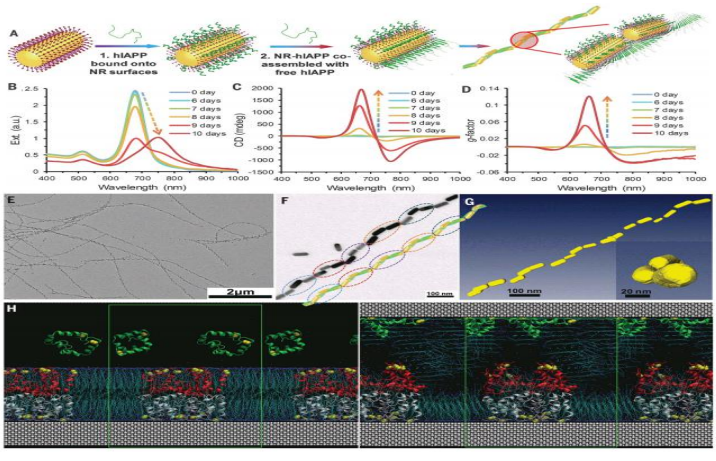

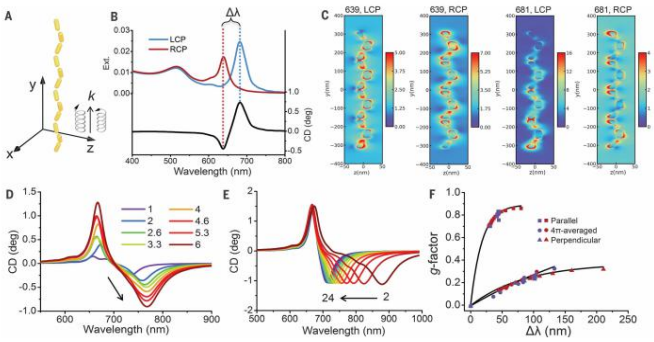

Fig. 2. Optical properties of NR helices with long-range registry. (A to C) Plasmonic resonances under circularly polarized light (CPL). (A) Nanohelix model with four helical turns and 12 NRs used for FDTD simulations with geometry based on cryo-TEM reconstructions. Extinction and CD spectra (B) are shown for the nanohelix and electric fields (C) irradiated at the extinction peaks under left- and right-handed CPL—i.e., 681 and 639 nm. deg, degrees. (D to F) Relationship of g-factor with Δλ. Simulated CD spectra for nanohelices with variable helical turns N (D) and interparticle distances d (E). (F) Dependence of g-factor on Δλ based on the simulation results for nanohelices with variable N (violet) and d (red) from the parallel (square), perpendicular (triangle), and 4π-averaged orientation (circle) with respect to the k-vector of incident photons.

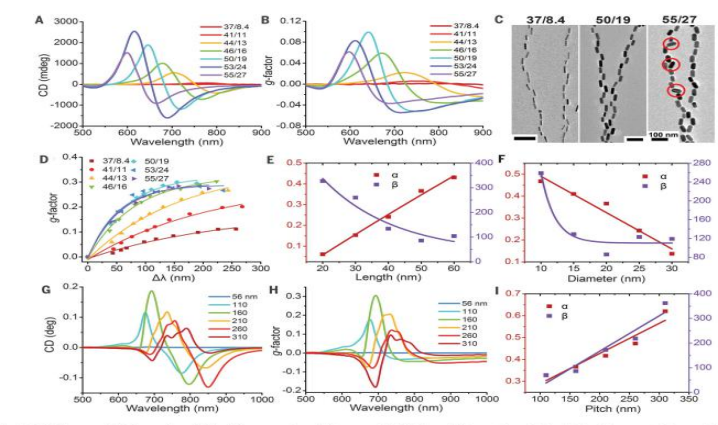

Fig. 3. The influence of NR size and nanohelix pitch on experimentally observed and computationally derived g-factors. (A to C) CD spectra (A), g-factor spectra (B), and representative TEM images (C) for helices from various sizes of NRs assembled under identical conditions. The numbers in the legends hIAPP fibers. (D) Dependence of simulated g-factors on Δλ for nanohelices from NRs of variable sizes. (E and F) Plot of α and β with NR lengths (E) and diameters (F) based on the g-factor dependence on Δλ for NRs and only changing the lengths or diameters, respectively. (G to I) Chiroptical properties of

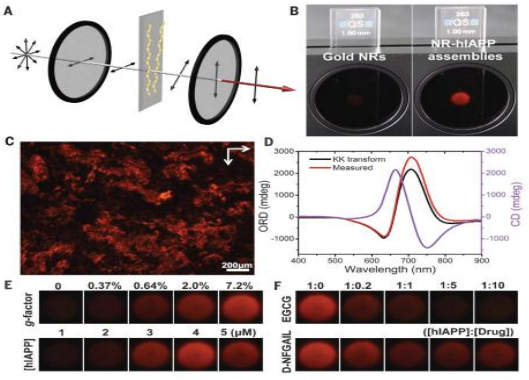

Fig. 4. Accelerated drug screening using high-g assemblies. (A) Schematics for cross-polarization optical cell being illuminated with LED light. NR-hIAPP assemblies are pictured being oriented perpendicularly to the k-vector of photons for simplicity; they form isotropic dispersions in biological media. (B) Photographs of pure NR and NR-hIAPP assemblies monitored by a camera and showing the red light transmitted under cross-polarized conditions. (C) Polarized optical microscopy (POM) image of NR-hIAPP assemblies. (D) Optical rotatory dispersion (ORD) spectrum of NR-hIAPP assemblies from the measurement and Kramers Kronig (KK) transformation to the corresponding CD spectra. (E and F) Photographs of the NR-hIAPP

[4]Scaling behavior of stiffness and strength of hierarchical network nanomaterials

分层网络纳米材料的刚度和强度的尺度特性

出版信息: Science 05 Mar 2021:Vol. 371, Issue 6533, pp. 1026-1033

作者：Shan Shi , Yong Li, Bao-Nam Ngo-Dinh, Jürgen Markmann, Jörg Weissmüller, et al.

第一作者单位：Institute of Materials Research, Materials Mechanics, Helmholtz-Zentrum Geesthacht, 21502 Geesthacht, Germany.

全文链接：https://science.sciencemag.org/content/371/6533/1026

Abstract：Structural hierarchy can enhance the mechanical behavior of materials and systems. This is exemplified by the fracture toughness of nacre or enamel in nature and by human-made architected microscale network structures. Nanoscale structuring promises further strengthening, yet macroscopic bodies built this way contain an immense number of struts, calling for scalable preparation schemes. In this work, we demonstrated macroscopic hierarchical network nanomaterials made by the self-organization processes of dealloying. Their hierarchical architecture affords enhanced strength and stiffness at a given solid fraction, and it enables reduced solid fractions by dealloying. Scaling laws for the mechanics and atomistic simulation support the observations. Because they expose the systematic benefits of hierarchical structuring in nanoscale network structures, our materials may serve as prototypes for future lightweight structural materials.

摘要翻译：结构层次可以增强材料和体系的力学性能。自然界中珍珠层或珐琅的断裂韧性以及人造的微尺度网状结构都证明了这一点。纳米尺度结构有望进一步强化，但以这种方式构建的宏观体包含了大量的支柱，需要可扩展的制备方案。

在这项研究中，我们展示了由自组织脱合金过程制备的宏观层次网络纳米材料。它们的层次结构在给定的固相分数下提供了增强的强度和刚度，并通过脱合金降低了固相分数。力学和原子模拟的标度定律支持这些观测结果。它们揭示了在纳米网络结构中分层结构的系统性好处，我们的材料可以作为未来轻型结构材料的原型。

文中插图：

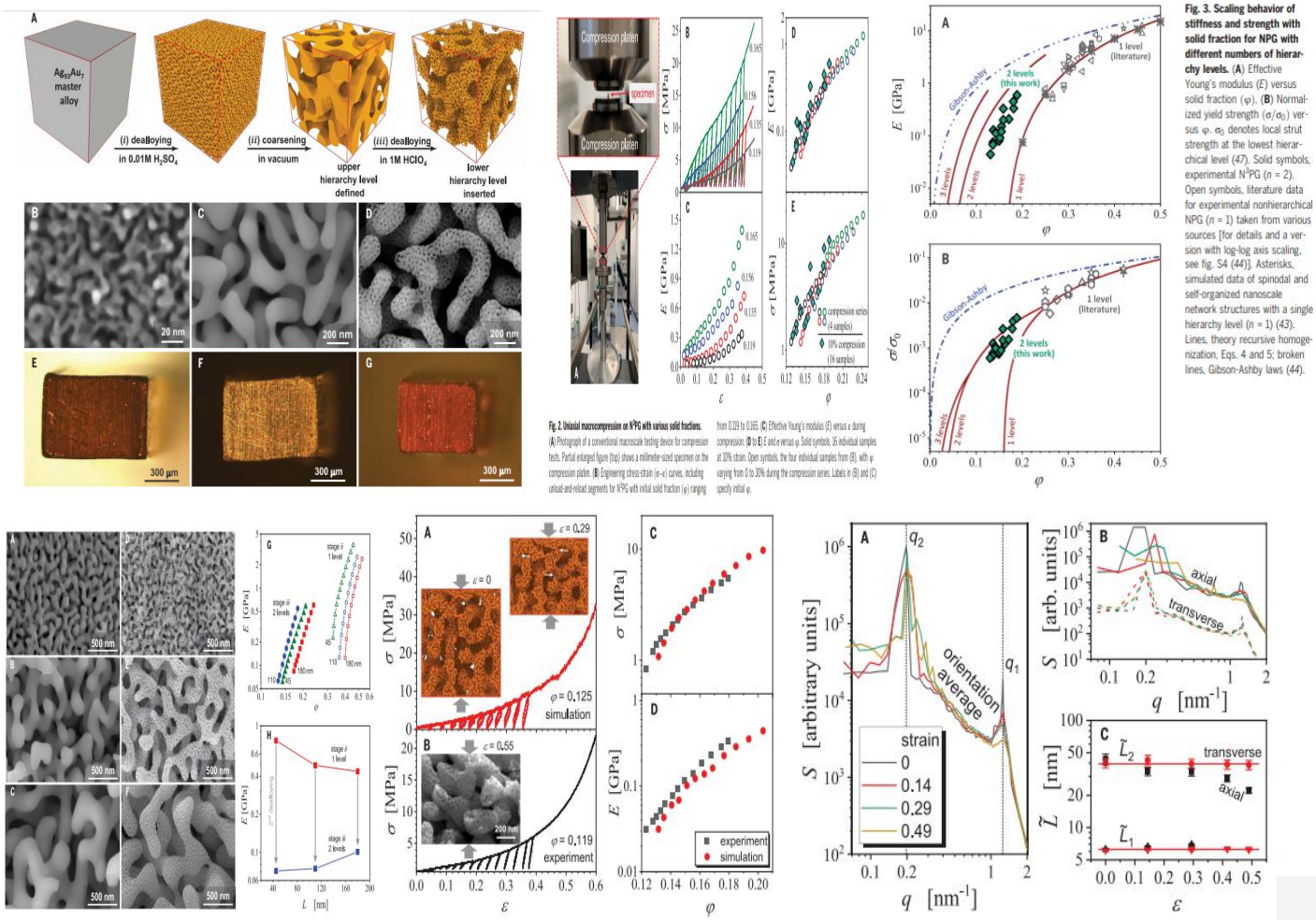

[5]Chiral-induced spin selectivity enables a room-temperature spin light-emitting diode

手性诱导自旋选择性助力室温自旋发光二极管

出版信息：Science　12 Mar 2021:Vol. 371, Issue 6534, pp. 1129-1133

作者：Young-Hoon Kim, Yaxin Zhai, Haipeng Lu, Xin Pan, Chuanxiao Xiao, E. Ashley Gaulding, et al.

第一作者单位：Chemistry and Nanoscience Center, National Renewable Energy Laboratory, Golden, CO 80401, USA.

全文链接：https://science.sciencemag.org/content/371/6534/1129

Abstract：In traditional optoelectronic approaches, control over spin, charge, and light requires the use of both electrical and magnetic fields. In a spin-polarized light-emitting diode (spin-LED), charges are injected, and circularly polarized light is emitted from spin-polarized carrier pairs. Typically, the injection of carriers occurs with the application of an electric field, whereas spin polarization can be achieved using an applied magnetic field or polarized ferromagnetic contacts. We used chiral-induced spin selectivity (CISS) to produce spin-polarized carriers and demonstrate a spin-LED that operates at room temperature without magnetic fields or ferromagnetic contacts. The CISS layer consists of oriented, self-assembled small chiral molecules within a layered organic-inorganic metal-halide hybrid semiconductor framework. The spin-LED achieves ±2.6% circularly polarized electroluminescence at room temperature.

摘要翻译：在传统的光电方法中，控制自旋、电荷和光需要同时使用电场和磁场。在自旋极化发光二极管（自旋 LED）中，电荷被注入，并且圆偏振光从自旋极化载流子对发射。典型载流子的注入发生在电场的应用中，而自旋极化可通过应用磁场或极化铁磁接触实现。研究组使用手性诱导自旋选择性（CISS）来产生自旋极化载流子，并展示了一种在室温下无磁场或铁磁接触的自旋发光二极管。CISS 层由定向的、自组装的手性小分子组成，它们位于层状有机-无机金属-卤化物杂化半导体框架内。自旋 LED 在室温下实现了±2.6%的圆极化电致发光。

文中插图：

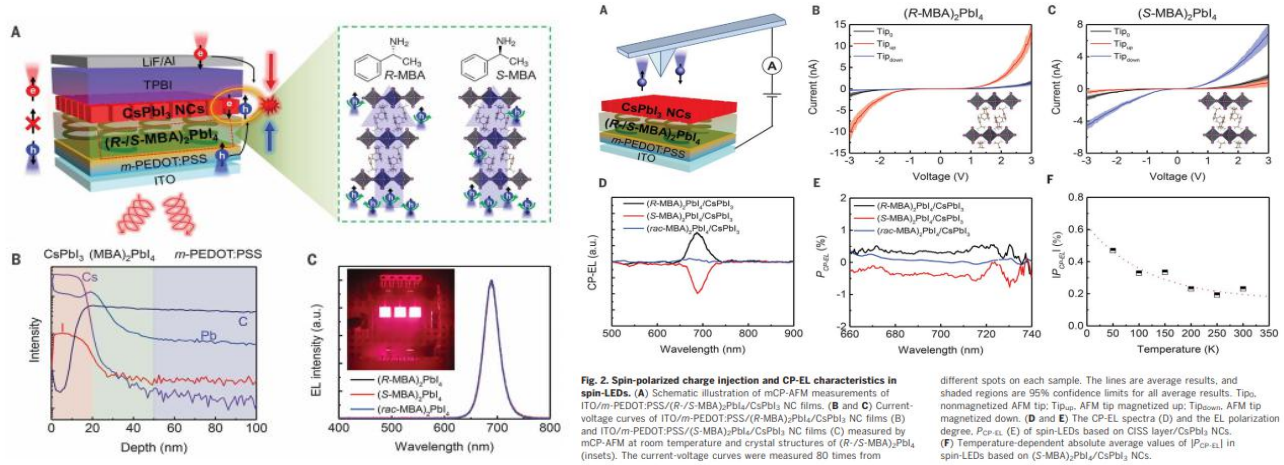

Fig. 2. Spin-polarized charge injection and CP-EL characteristics in spin-LEDs. (**A**) Schematic illustration of mCP-AFM measurements of ITO/*m*-PEDOT:PSS/(*R*-/*S*-MBA)$_2$PbI$_4$/CsPbI$_3$ NC films. (**B** and **C**) Current-voltage curves of ITO/*m*-PEDOT:PSS/(*R*-MBA)$_2$PbI$_4$/CsPbI$_3$ NC films (B) and ITO/*m*-PEDOT:PSS/(*S*-MBA)$_2$PbI$_4$/CsPbI$_3$ NC films (C) measured by mCP-AFM at room temperature and crystal structures of (*R*-/*S*-MBA)$_2$PbI$_4$ (insets). The current-voltage curves were measured 80 times from different spots on each sample. The lines are average results, and shaded regions are 95% confidence limits for all average results. Tip$_{\uparrow}$, nonmagnetized AFM tip; Tip$_{down}$, AFM tip magnetized up; Tip$_{down}$, AFM tip magnetized down. (**D** and **E**) The CP-EL spectra (D) and the EL polarization degree, $P_{CP\text{-}EL}$ (E) of spin-LEDs based on CISS layer/CsPbI$_3$ NCs. (**F**) Temperature-dependent absolute average values of $|P_{CP\text{-}EL}|$ in spin-LEDs based on (*S*-MBA)$_2$PbI$_4$/CsPbI$_3$ NCs.

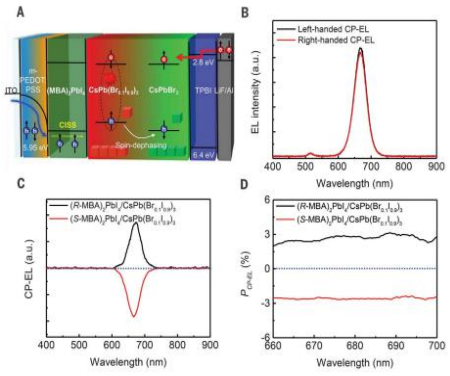

Fig. 3. CP-EL from mixed halide perovskite NCs. (**A**) Schematic illustration of hole injection through ITO/*m*-PEDOT:PSS (blue arrow), spin-polarized hole injection through CISS layer (yellow arrow), unpolarized electron injection through TPBI/LiF/Al (red arrow), spin dephasing (white arrow), and formation of mixed halide perovskites under the electric field and generation of CP-EL (dashed circle) in the spin-LEDs. (**B**) Left-handed and right-handed CP-EL spectrum of spin-LEDs based on (*R*-MBA)$_2$PbI$_4$/CsPbBr$_3$ NC heterostructure. (**C** and **D**) CP-EL (C) and $P_{CP\text{-}EL}$ (D) of spin-LEDs based on CISS layer/CsPbBr$_3$ NC heterostructure.

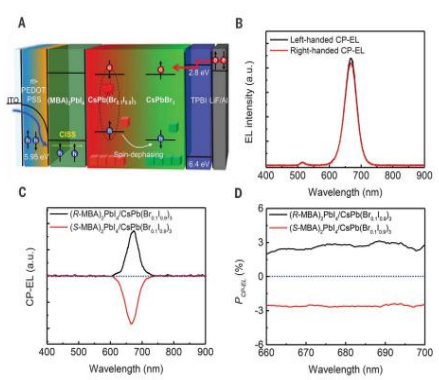

Fig. 3. CP-EL from mixed halide perovskite NCs. (**A**) Schematic illustration of hole injection through ITO/*m*-PEDOT:PSS (blue arrow), spin-polarized hole injection through CISS layer (yellow arrow), unpolarized electron injection through TPBI/LiF/Al (red arrow), spin dephasing (white arrow), and formation of mixed halide perovskites under the electric field and generation of CP-EL (dashed circle) in the spin-LEDs. (**B**) Left-handed and right-handed CP-EL spectrum of spin-LEDs based on (*R*-MBA)$_2$PbI$_4$/CsPbBr$_3$ NC heterostructure. (**C** and **D**) CP-EL (C) and $P_{CP\text{-}EL}$ (D) of spin-LEDs based on CISS layer/CsPbBr$_3$ NC heterostructure.

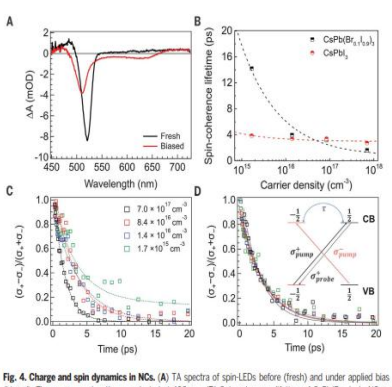

Fig. 4. Charge and spin dynamics in NCs. (**A**) TA spectra of spin-LEDs before (fresh) and under applied bias (biased). The pump wavelength was selected at 400 nm. (**B**) Spin-coherence lifetime of CsPb(Br$_{0.5}$I$_{0.5}$)$_3$ NC and CsPbI$_3$ NC films measured at different excitation carrier densities. The dashed lines are fitted curves of carrier density–dependent spin lifetimes determined using a conventional power law (*33*, *34*). (**C** and **D**) Spin-coherence dynamics in CsPb(Br$_{0.5}$I$_{0.5}$)$_3$ NC films (C) and CsPbI$_3$ NC films (D) measured at different excitation carrier densities. Inset in (D) is the mechanism of spin-coherence lifetime measurement. Pump σ_+ (black) has angular momentum of $|+1\rangle$ and generates a m_j polarization, whereas pump σ_- (red) does the opposite. The probe σ_+ pulse selectively detects the change in spin polarization. The flip of a spin will simultaneously lead to a decay of the σ_+ bleach and a formation of the σ_- bleach. CB, conduction band; VB, valence band.

[6]Electric field－tunable superconductivity in alternating-twist magic-angle trilayer graphene

交变扭转魔角三层石墨烯的电场可调超导性

出版信息：Science　12 Mar 2021:Vol. 371, Issue 6534, pp. 1133-1138

作者：Zeyu Hao, A. M. Zimmerman, Patrick Ledwith, Eslam Khalaf, Danial Haie Najafabadi, Kenji Watanabe, et al.

第一作者单位：Department of Physics, Harvard University, Cambridge, MA 02138, USA.

全文链接：https://science.sciencemag.org/content/371/6534/1133

Abstract：Engineering moiré superlattices by twisting layers in van der Waals (vdW) heterostructures has uncovered a wide array of quantum phenomena. We constructed a vdW heterostructure that consists of three graphene layers stacked with alternating twist angles $\pm\theta$. At the average twist angle $\theta \sim 1.56°$, a theoretically predicted "magic angle" for the formation of flat electron bands, we observed displacement field－tunable superconductivity with a maximum critical temperature of 2.1 kelvin. By tuning the doping level and displacement field, we found that superconducting regimes occur in conjunction with flavor polarization of moiré bands and are bounded by a van Hove singularity (vHS) at high displacement fields. Our findings display inconsistencies with a weak coupling description, suggesting that the observed moiré superconductivity has an unconventional nature.

摘要翻译：工程学莫尔超晶格通过扭转范德华（vdW）异质结构中的层，揭示了一系列广泛的量子现象。研究组构建了一种 vdW 异质结构，由三层交错扭角 $\pm\theta$ 的石墨烯层组成。在平均扭角 $\theta \sim 1.56°$ 时，即理论上预测的形成平坦电子带的"魔角"，研究组观察到位移场-可调超导性，最高临界温度为 2.1 开尔文。通过调谐掺杂能级和位移场，研究组发现超导机制与莫尔带的极化一同出现，并且在高位移场中受到范·霍伍奇异点（vHS）的限制。研究组的发现与弱耦合描述不一致，这表明观察到的莫尔超导电性具有非常规性质。

文中插图：

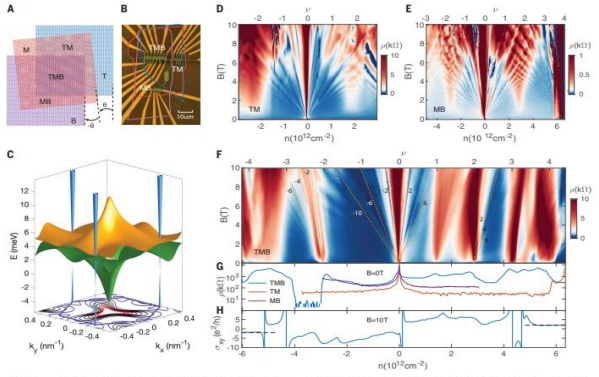

Fig. 1. Device structure and characterization. (**A**) Schematic diagram of the three layers of TTG with alternating twist angles θ and −θ. The top and bottom layers are aligned with each other, whereas the middle layer is twisted by θ relative to both layers, preserving the in-plane mirror symmetry. (**B**) Optical microscope image of the TTG device fabricated in the TMB region and two TBG devices fabricated in the TM and MB regions. (**C**) Theoretical band structure for MA-TTG at $D/\epsilon_0 = 0$ plotted on the mini Brillouin zone (BZ), marked in purple in the bottom face. The blue Dirac cones sit at the mini BZ *K* points, whereas the flat bands, orange (conduction) and green (valence), are the most dispersive at the mini BZ Γ point. A contour plot of the valence band is projected on the *x*-*y* plane. (**D** and **E**) Landau fan diagrams of the two TBG Hall bars TM and MB. In each device, fans are visible emanating from $\nu = 0$ and $\nu = \pm 4$ as well as an increase in resistance at the vHSs near $\nu = \pm 2$. (**F**) Landau fan diagram of the TTG Hall bar TMB. Resistive states and fans emerge at $\nu = 0, \pm 1, \pm 2$, and ±3. The most prominent sequences are traced out with orange dashed lines (fig. S5). (**G**) Zero magnetic field resistivity as a function of filling in TM, MB, and TMB. (**H**) Hall conductivity in TMB at $B = 10$ T.

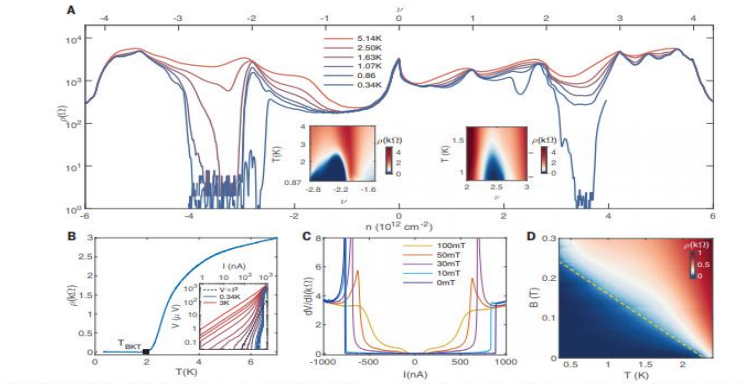

Fig. 2. Superconductivity in TTG. (**A**) ρ as a function of ν taken at a fixed back gate voltage $V_{BG} = 0$ V at several different temperature values. The formation of superconducting regions is visible at $\nu < -2$ and $\nu > 2$. (Insets) The superconducting dome in the *T*-ν plane taken along a cut at (left inset) $V_{BG} = 0$ V for $\nu < -2$ and (right inset) at $D/\epsilon_0 = -0.56$ V/nm for $\nu > 2$. (**B**) Superconducting transition in resistivity at $\nu = -2.3$ and $D/\epsilon_0 = 0.29$ V/nm. The BKT transition temperature T_{BKT} is indicated with the black square. (Inset) *I*-*V* characteristic of the superconductor from 0.34 K (blue) to 3 K (red) on a log-log scale, displaying a crossover from high-power polynomial to linear behavior in the low *V* range. The black dashed line indicates where $V \propto I^3$, defining T_{BKT}. (**C**) Differential resistance as a function of dc bias current at different magnetic fields. (**D**) ρ as a function of temperature and perpendicular magnetic field at $\nu = -2.3$ and $D/\epsilon_0 = 0.4$ V/nm. The dashed line corresponds to a GL theory fit with a coherence length of $\xi_{GL} = 34$ nm (*31*).

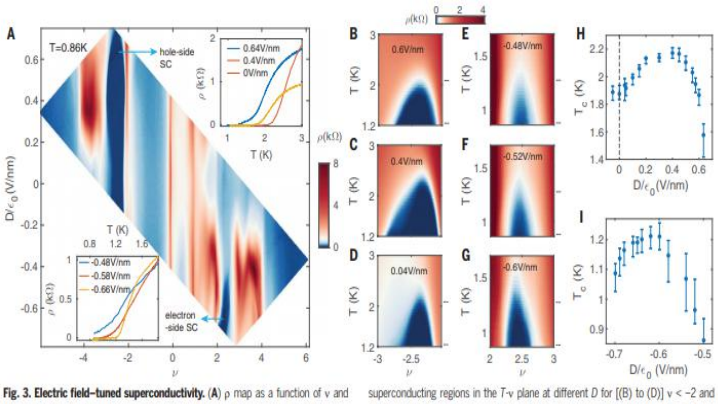

Fig. 3. Electric field–tuned superconductivity. (**A**) ρ map as a function of ν and *D* at 0.86 K. Superconducting regions appear for $\nu < -2$ and $\nu > 2$. (Top inset) The ρ at the superconducting transition in the hole region. (Bottom inset) The ρ at the superconducting transition in the electron region. (**B** to **G**) Dome-shaped superconducting regions in the *T*-ν plane at different *D* for [(B) to (D)] $\nu < -2$ and [(E) to (G)] $\nu > 2$. The size and shape of the domes are tuned by *D*. (**H** and **I**) T_c as a function of *D* taken at (H) $\nu = -2.3$ and (I) $\nu = 2.45$. T_c is chosen to be the point at which $\rho = 10\%\ \rho_N$, and error bars correspond to 5% ρ_N and 15% ρ_N.

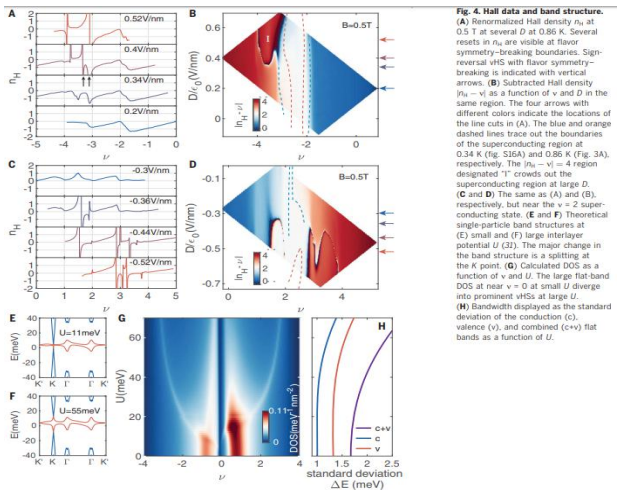

Fig. 4. Hall data and band structure. (**A**) Renormalized Hall density n_H at 0.5 T at several *D* at 0.86 K. Several resets in n_H are visible at flavor symmetry–breaking boundaries. Sign-reversal vHS with flavor symmetry–breaking is indicated with vertical arrows. (**B**) Subtracted Hall density $|n_H - \nu|$ as a function of ν and *D* in the same region. The four arrows with different colors indicate the locations of the line cuts in (A). The blue and orange dashed lines trace out the boundaries of the superconducting region at 0.34 K (fig. S16A) and 0.86 K (Fig. 3A), respectively. The $|n_H - \nu| = 4$ region designated "I" crowds out the superconducting region at large *D*. (**C** and **D**) The same as (A) and (B), respectively, but near the $\nu = 2$ superconducting state. (**E** and **F**) Theoretical single-particle band structures at (E) small and (F) large interlayer potential *U* (*31*). The major change in the band structure is a splitting at the *K* point. (**G**) Calculated DOS as a function of ν and *U*. The large flat-band DOS at near $\nu = 0$ at small *U* diverge into prominent vHSs at large *U*. (**H**) Bandwidth displayed as the standard deviation of the conduction (c), valence (v), and combined (c+v) flat bands as a function of *U*.

[1]Macroscopic materials assembled from nanoparticle superlattices

纳米颗粒超晶格组装的宏观材料

出版信息：Nature 18 March 2021：Vol 591, pages586－591(2021)

作者：Peter J. Santos, Paul A. Gabrys, Leonardo Z. Zornberg, Margaret S. Lee & Robert J. Macfarlane

第一作者单位：Department of Materials Science and Engineering, Massachusetts Institute of Technology, Cambridge, MA, USA

全文链接：https://www.nature.com/articles/s41586-021-03355-z

Abstract：Nanoparticle assembly has been proposed as an ideal means to program the hierarchical organization of a material by using a selection of nanoscale components to build the entire material from the bottom up. Multiscale structural control is highly desirable because chemical composition, nanoscale ordering, microstructure and macroscopic form all affect physical properties. However, the chemical interactions that typically dictate nanoparticle ordering do not inherently provide any means to manipulate structure at larger length scales. Nanoparticle-based materials development therefore requires processing strategies to tailor micro- and macrostructure without sacrificing their self-assembled nanoscale arrangements. Here we demonstrate methods to rapidly assemble gram-scale quantities of faceted nanoparticle superlattice crystallites that can be further shaped into macroscopic objects in a manner analogous to the sintering of bulk solids. The key advance of this method is that the chemical interactions that govern nanoparticle assembly remain active during the subsequent processing steps, which enables the local nanoscale ordering of the particles to be preserved as the macroscopic materials are formed. The nano- and microstructure of the bulk solids can be tuned as a function of the size, chemical makeup and crystallographic symmetry of the superlattice crystallites, and the micro- and macrostructures can be controlled via subsequent processing steps. This work therefore provides a versatile method to simultaneously control structural organization across the molecular to macroscopic length scales.

摘要翻译：纳米颗粒组装被认为是一种规划材料层次结构的理想方法，通过选择纳米尺度的组件，自下而上构建整个材料。多尺度结构控制是非常可取的，因为化学成分、纳米尺度排序、微观结构和宏观形态都会影响物理性能。然而，通常决定纳米颗粒排序的化学相互作用本身，并不能提供任何手段来在更大的长度尺度上操纵结构。因此，基于纳米颗粒材料的研发需要在不牺牲其自组装的纳米尺度排列情况下，采用加工策略来定制微观和宏观结构。研究组展示了快速组装克级数量的多面纳米颗粒超晶格晶体的方法，这些纳米颗粒可以进一步形成宏观物体，其方式类似于块状固体的烧结。这种方法的关键是控制纳米颗粒组装的化学相互作用在后续加工过程中保持活跃，这使得颗粒的局部纳米级有序性在形成宏观材料时得以保持。大块固体的纳米和微观结构可以根据超晶格晶粒的尺寸、化学组成和晶体对称性进行调节，微观和宏观结构可以通过后续的处理步骤进行控制。因此，这项工作提供了一种通用方法，可同时控制从分子到宏观长度尺度的结构组织。

文中插图：

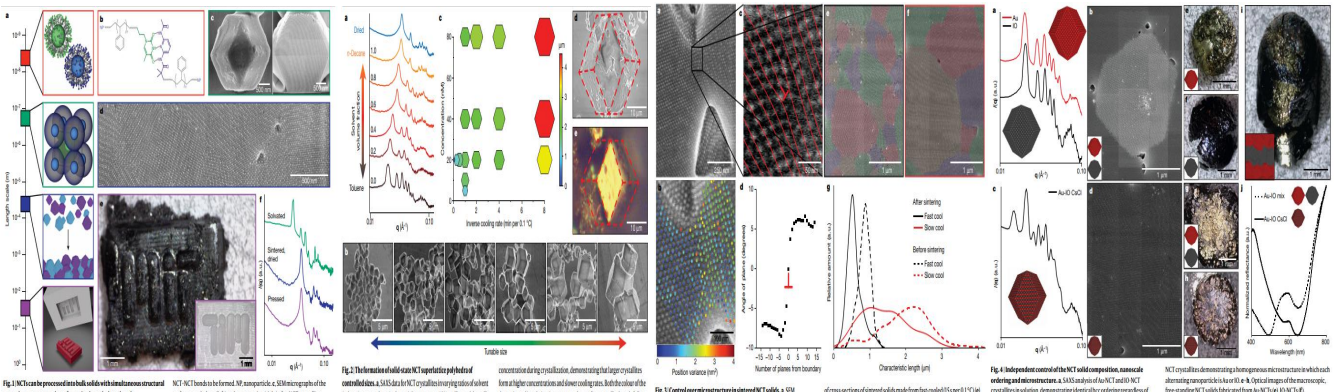

[2]High-order superlattices by rolling up van der Waals heterostructures

卷起来的范德华异质结构的高阶超晶格

出版信息：Nature 18 March 2021：Vol 591 , 385 – 390

作者：Bei Zhao, Zhong Wan, Yuan Liu, Junqing Xu, et al.

第一作者单位：Hunan Key Laboratory of Two-Dimensional Materials, State Key Laboratory for Chemo/Biosensing and Chemometrics, College of Chemistry and Chemical Engineering, Hunan University, Changsha, China

国内相关报道：http://cc.hnu.edu.cn/info/1058/8888.htm

全文链接：https://www.nature.com/articles/s41586-021-03338-0

Abstract：Two-dimensional (2D) materials and the associated van der Waals (vdW) heterostructures have provided great flexibility for integrating distinct atomic layers beyond the traditional limits of lattice-matching requirements, through layer-by-layer mechanical restacking or sequential synthesis. Here we report a straightforward approach to realizing high-order vdW superlattices by rolling up vdW heterostructures. We show that a capillary-force-driven rolling-up process can be used to delaminate synthetic SnS2/WSe2 vdW heterostructures from the growth substrate and produce SnS2/WSe2 roll-ups with alternating monolayers of WSe2 and SnS2, thus forming high-order SnS2/WSe2 vdW superlattices. The formation of these superlattices modulates the electronic band structure and the dimensionality, resulting in a transition of the transport characteristics from semiconducting to metallic, from 2D to one-dimensional (1D), with an angle-dependent linear magnetoresistance. This study demonstrates a general approach to producing high-order vdW superlattices with widely variable material compositions, dimensions, chirality and topology, and defines a rich material platform for both fundamental studies and technological applications.

摘要翻译：二维材料和相关的范德华（vdW）异质结构为集成不同的原子层提供了极大的灵活性，超越了传统晶格匹配要求的限制，可以逐层机械堆叠或顺序合成。在此，我们报告了一种通过卷起范德华异质结构来实现高阶范德华超晶格的直接方法。我们的研究表明，毛细作用力驱动的卷绕过程可用于从生长基质上剥离合成的 SnS2/WSe2 vdW 异质结构，并产生具有交替的 WSe2 和 SnS2 单层的 SnS2/WSe2 卷绕，从而形成高阶 SnS2/WSe2 vdW 超晶格。这些超晶格的形成调制了电子带结构和尺寸，导致输运特性从半导体到金属、从二维到一维以及与角度相关的线性磁阻转变。本研究展示了一种生成高阶 vdW 超晶格的通用方法，该超晶格具有广泛的材料组成、尺寸、手性和拓扑结构，并为基础研究和技术应用定义了丰富的材料平台。

文中插图：

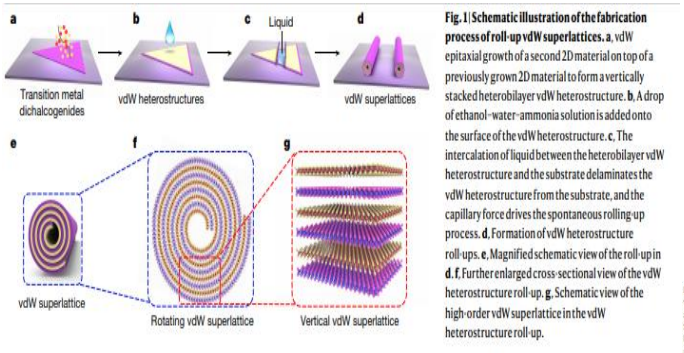

Fig. 1 | Schematic illustration of the fabrication process of roll-up vdW superlattices. **a**, vdW epitaxial growth of a second 2D material on top of a previously grown 2D material to form a vertically stacked heterobilayer vdW heterostructure. **b**, A drop of ethanol–water–ammonia solution is added onto the surface of the vdW heterostructure. **c**, The intercalation of liquid between the heterobilayer vdW heterostructure and the substrate delaminates the vdW heterostructure from the substrate, and the capillary force drives the spontaneous rolling-up process. **d**, Formation of vdW heterostructure roll-ups. **e**, Magnified schematic view of the roll-up in **d**. **f**, Further enlarged cross-sectional view of the vdW heterostructure roll-up. **g**, Schematic view of the high-order vdW superlattice in the vdW heterostructure roll-up.

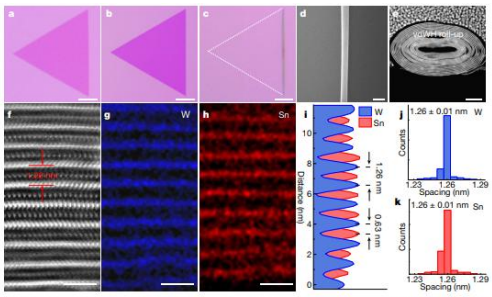

Fig. 2 | Structural characterizations of SnS_2/WSe_2 roll-ups and high-order vdW superlattices. **a**–**c**, Optical microscopy images of a WSe_2 monolayer (**a**), a SnS_2/WSe_2 heterobilayer vdW heterostructure (**b**) and a SnS_2/WSe_2 roll-up (**c**). Scale bars, 10 μm. **d**, SEM image of a representative SnS_2/WSe_2 roll-up. Scale bar, 200 nm. **e**, Cross-sectional STEM image of a representative SnS_2/WSe_2 roll-up. Scale bar, 20 nm. **f**, Higher-resolution cross-sectional STEM image of the SnS_2/WSe_2 vdW superlattice. The bright and dark regions correspond to the WSe_2 and SnS_2 monolayers, respectively. Scale bar, 2 nm. **g**, **h**, Corresponding EDS mapping images for W (**g**) and Sn (**h**). Scale bars, 2 nm. **i**, EDS intensity profiles for W (blue) and Sn (red). **j**, **k**, Statistical distribution of interlayer spacing between W atoms (**j**) and Sn atoms (**k**).

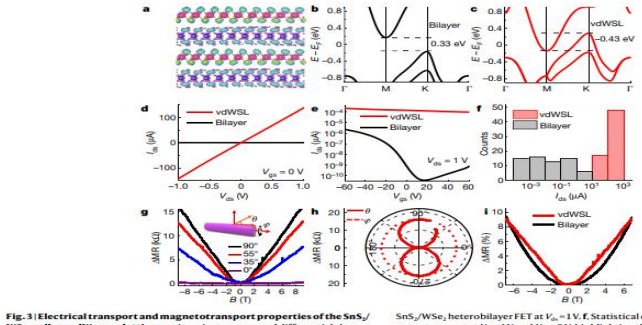

Fig. 3 | Electrical transport and magnetotransport properties of the SnS_2/WSe_2 roll-up vdW superlattices. **a**, Atomic structure and differential charge density calculated for the SnS_2/WSe_2 vdW superlattice. The amaranth and blue isosurfaces represent negative and positive charge density differences, respectively, between the vdW superlattice and the separated layers. The SnS_2/WSe_2 heterobilayer FET at $V_{bg} = 1$ V. **f**, Statistical distribution of the output current at $V_{bg} = 1$ V and $V_{ds} = 0$ V, highlighting that the SnS_2/WSe_2 roll-up FETs show considerably higher conductance than the heterobilayers. **g**, Magnetoresistance (ΔMR) of roll-up vdW superlattices with different rotation angles θ at $T = 3$ K. Inset, schematic drawing of the roll-up vdW superlattices, and

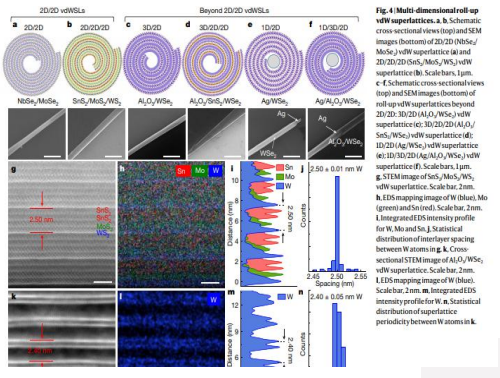

Fig. 4 | Multi-dimensional roll-up vdW superlattices. **a**, **b**, Schematic cross-sectional views (top) and SEM images (bottom) of 2D/2D ($NbSe_2/MoSe_2$) vdW superlattice (**a**) and 2D/2D/2D ($SnS_2/MoS_2/WS_2$) vdW superlattice (**b**). Scale bars, 1 μm. **c**–**f**, Schematic cross-sectional views (top) and SEM images (bottom) of roll-up vdW superlattices beyond 2D/2D: 3D/2D (Al_2O_3/WSe_2) vdW superlattice (**c**); 3D/2D/2D ($Al_2O_3/SnS_2/WSe_2$) vdW superlattice (**d**); 1D/2D (Ag/WSe_2) vdW superlattice (**e**); 1D/3D/2D (Ag/Al_2O_3/WSe_2) vdW superlattice (**f**). Scale bars, 1 μm. **g**, STEM image of $SnS_2/MoS_2/WS_2$ vdW superlattice. Scale bar, 2 nm. **h**, EDS mapping image of W (blue), Mo (green) and Sn (red). Scale bar, 2 nm. **i**, Integrated EDS intensity profile for W, Mo and Sn. **j**, Statistical distribution of interlayer spacing between W atoms in **g**. **k**, Cross-sectional STEM image of Al_2O_3/WSe_2 vdW superlattice. Scale bar, 2 nm. **l**, EDS mapping image of W (blue). Scale bar, 2 nm. **m**, Integrated EDS intensity profile for W. **n**, Statistical distribution of superlattice periodicity between W atoms in **k**.

[3]Ligand-engineered bandgap stability in mixed-halide perovskite LEDs

混合卤化物钙钛矿 LED 配体设计的带隙稳定性

出版信息：Nature　18 March 2021：Vol 591 , 72 – 77

作者： Yasser Hassan, Jong Hyun Park, Michael L. Crawford, Aditya Sadhanala, Jeongjae Lee, James C. Sadighian, et al.

第一作者单位：Clarendon Laboratory, Department of Physics, University of Oxford, Oxford, UK

全文链接：https://www.nature.com/articles/s41586-021-03217-8

Abstract：Lead halide perovskites are promising semiconductors for light-emitting applications because they exhibit bright, bandgap-tunable luminescence with high colour purity. Owing to the formation of lower-bandgap iodide-rich domains, efficient and colour-stable red electroluminescence from mixed-halide perovskites has not yet been realized. Here we report the treatment of mixed-halide perovskite nanocrystals with multidentate ligands to suppress halide segregation under electroluminescent operation. We demonstrate colour-stable, red emission centred at 620 nanometres, with an electroluminescence external quantum efficiency of 20.3 per cent. We show that a key function of the ligand treatment is to ‘clean’ the nanocrystal surface through the removal of lead atoms. Density functional theory calculations reveal that the binding between the ligands and the nanocrystal surface suppresses the formation of iodine Frenkel defects, which in turn inhibits halide segregation. Our work exemplifies how the functionality of metal halide perovskites is extremely sensitive to the nature of the (nano)crystalline surface and presents a route through which to control the formation and migration of surface defects. This is critical to achieve bandgap stability for light emission and could also have a broader impact on other optoelectronic applications—such as photovoltaics—for which bandgap stability is required.

摘要翻译：卤化铅钙钛矿是一种很有前途的半导体发光材料，因为它们具有明亮的、带隙可调的高纯色发光。由于低带隙富碘化物畴的形成，混合卤化物钙钛矿尚未实现有效、颜色稳定的红色电致发光。研究组报道了用多齿配体处理混合卤化物钙钛矿纳米晶体以抑制电致发光操作下的卤化物偏析。他们展示了颜色稳定的红色发射，中心波长为 620 纳米，电致发光外量子效率为 20.3%。研究组证明配体处理的一个关键功能是通过去除铅原子来“清洁”纳米晶体表面。密度泛函理论计算表明，配体与纳米晶体表面的结合抑制了碘弗伦克尔缺陷的形成，从而抑制了卤化物的偏析。研究组的工作举例说明了金属卤化物钙钛矿的功能性如何对（纳米）晶体表面的性质极其敏感，并提出了一个控制表面缺陷形成和迁移的途径。这对于实现光发射的带隙稳定性至关重要，也可能对其他需要带隙稳定的光电应用产生更广泛的影响，例如光伏。

文中插图：